

Accelerated Degradation of All-Solid-State Batteries Induced through Volumetric Occupation of the Carbon Additive in the Solid Electrolyte Domain

Hyun-seung Kim, Sejin Park, Sora Kang, Jae Yup Jung, KyungSu Kim, Ji-Sang Yu, Dong-Won Kim, Jong-Won Lee,* Yang-Kook Sun,* and Woosuk Cho*

The accelerated oxidative degradation observed in all-solid-state batteries (ASSBs), particularly focusing on the argyrodite solid electrolyte in conjunction with Ni-rich positive electrode surfaces is demonstrated. The formation of oxidative intermediates of the solid electrolyte oxidation process increases the amount of oxidation on the NCM surface with conductive carbon. The introduction of high-weight-composition conductive carbon additives results in a reduction of solid electrolytes within the positive electrode and the amount of solid electrolytes retained after formation. Consequently, cells with high concentrations of carbon additives demonstrate a decrease in both the cycle and power performances of ASSBs. The energy density of ASSBs is significantly limited by the fundamental failure mechanism induced by conductive carbon, particularly pronounced in cells with high active material contents. Consequently, this study provides pivotal insights for the design of high-energy-density ASSBs with NCM electrodes and high active material contents. To mitigate failure induced by high-volumetric-occupied carbon additives, carbon fiber-type additives are further utilized to interconnect the NCMs by decreasing the occupation of the solid electrolyte domain by carbon. Morphological alteration of the carbon additive significantly improves the electrochemical performance of ASSBs by preventing the deterioration of the electrode structure even after prolonged cycling and suppressing electrolyte degradation.

lithium secondary batteries; hence, all-solid-state batteries (ASSBs) are highly promising as post-lithium-ion batteries (LIB) owing to their advanced electrochemical performance.^[1] The solid electrolyte in cutting-edge ASSBs should possess high ionic conductivity and processability; thus, argyrodite-based sulfide solid electrolyte systems are promising solid electrolytes for high-energy post-LIBs.^[1b,2] Since the potential application of the high energy ASSB is the electric vehicles, the rate performances are should be satisfied to assure the acceleration and fast-charging of batteries;^[3] which is typically improved with the carbon additive incorporation.^[4] However, the significant oxidative decomposition of the sulfide electrolyte upon contact with the surface of the carbon additives and positive electrode has been identified as the principal failure mechanism. Thus, mitigating the degradation of the ASSBs requires detailed interfacial modulation.^[1i,5] Typically, techniques such as coating the active material and modifying the surface properties of the synthesized positive active material are employed to enhance the electrochemical performance

of positive electrodes.^[1c,e,3b,5a,6] While the anodic side reaction of the solid electrolyte at the Ni-rich positive electrodes (NCM) is mitigated by surface manipulation,^[1e,i,6b,7] suppression of electrolyte oxidation on the conductive carbon surface has recently been achieved.^[4a,8] A typical strategy to reduce electrolyte

1. Introduction

The substitution of conventional liquid electrolytes with highly ionic conductive solid electrolytes has been intensively conducted to simultaneously enhance the energy density and safety of

H.-s. Kim, S. Park, S. Kang, J. Y. Jung, K. Kim, J.-S. Yu, W. Cho
Advanced Batteries Research Center
Korea Electronics Technology Institute
25, Saenari-ro, Seongnam 13509, Republic of Korea
E-mail: cho4153@keti.re.kr

S. Park, D.-W. Kim
Department of Chemical Engineering
Hanyang University
222 Wangsimni-ro, Seongdong-gu, Seoul 04763, Republic of Korea

J.-W. Lee
Division of Materials Science and Engineering
Hanyang University
222 Wangsimni-ro, Seongdong-gu, Seoul 04763, Republic of Korea
E-mail: jongwonlee@hanyang.ac.kr

Y.-K. Sun
Department of Energy Engineering
Hanyang University
222 Wangsimni-ro, Seongdong-gu, Seoul 04763, Republic of Korea
E-mail: yksun@hanyang.ac.kr

 The ORCID identification number(s) for the author(s) of this article can be found under <https://doi.org/10.1002/adfm.202409318>

DOI: 10.1002/adfm.202409318

decomposition on the carbon surface involves coating carbon additives with insulating materials;^[8a,c] thus, the effectiveness of the carbon additive is subsequently degraded by the insulating surface properties. Consequently, a detailed understanding of the failure mechanism induced by conductive carbon additives is required to improve the ASSBs performance.

The oxidative decomposition of the argyrodite solid electrolyte on the NCM surface is facilitated by the coupled oxidation of the solid electrolyte. This oxidation process on the conductive carbon readily generates oxidative intermediates, leading to significant oxidation of the NCM surface. The incorporation of a high-weight composition of conductive carbon additives reduces the proportion of solid electrolytes in the positive electrode sector and preserves the solid electrolyte after the formation of the NCM electrode. Consequently, the failure of the cycle and power performance of the ASSBs occurred significantly in the high-carbon-additive-content cells. This conductive carbon-induced failure mechanism is observed in highly active material-contented cells, which significantly limits the energy density of ASSBs as the volumetric occupation of conductive carbon is relatively increased, particularly in electrodes comprising over 90 wt% of active material. In general, the reported typical failure mechanisms at the high-energy dry electrodes are the void formation, particle cracking of positive active materials induced diffusion limitation after calendaring process.^[9] Thus the improvement strategies is mainly based on the enhancement of mechanical deterioration. Thus, this study provides crucial insights into the design of high-energy-density ASSBs with Ni-rich and high active-material ratios comprising practical electrodes. To mitigate ASSB failure resulting from the high volumetric occupation of the conductive carbon additives, the line connection of the active materials was performed with carbon fiber-type additives. This morphological change in the conductive carbon additive significantly enhances the electrochemical performance of ASSBs by suppressing electrolyte decomposition, while preserving the electrode structure integrity after prolonged cycling.

2. Results and Discussion

To enhance the specific and volumetric capacities of the positive electrode, it is crucial to increase the proportion of active material in the electrode. Hence, the electrochemical and physicochemical characterizations of the positive active material portion-dependent powder electrodes were performed (Figure 1). Each cell maintains a constant value of 3 wt% of carbon additive (spherical carbon, SC), exhibiting increased polarization at the highly active material-contented cell (Figure 1a). At 90 wt% of active material content, a noticeable polarization was observed, leading to a 2.0% decrease in Coulombic efficiency compared to cells containing 80 and 85 wt% of active materials. The rate performance of the ASSBs showed well-retained lithiation capacity at 80 and 85 wt% cells, while at 90 wt%, the capacity significantly diminished even with 0.5 C-rate (Figure 1b). Voltage profiles dependent on the C-rate displayed abnormal polarization growth in cells with 90 wt% active material, contrasting with the well-preserved profiles of cells containing 80 and 85 wt%. (Figure S1, Supporting Information) Thus a distinct failure mechanism is observed in cells with 90 wt% active material. Notably, the ionic conductivities of the powder electrode significantly decreased at

90 wt% cell (Figure 1c). The electrical conductivity of the powder electrode (Figure 1d) increased gradually with increasing active-material composition because the electrical conductivity of the active material is higher than that of the solid electrolyte. Thus, the decrease in ionic conductivity significantly affected the electrochemical performance of the ASSBs at 90 wt% positive active material composition, reaching one-tenth of that of 80 wt. % electrode. The volumetric occupation diagram and its effect on the high-active-material-content powder electrode are shown in Figure 1e. As the active material composition increased, the fraction of solid electrolytes decreased while maintaining a constant introduction of carbon additive, leading to a substantial decline in the volumetric fraction of solid electrolytes from 30.0 vol. % to 13.9 vol. % for 80 wt% and 90 wt% of active materials, respectively. Further, the densities of the solid electrolyte and conductive carbon additive were measured by Archimedes method at isopropyl alcohol. The measured density was 1.86 g cm⁻³ for sulfide electrolyte and 0.67 g cm⁻³ for SC. Hence the substitution of the sulfide electrolyte by the SC additive greatly increases the occupation of carbon additive in the solid electrolyte domain, implying that the solid electrolyte and NCM is highly contacted with carbon surface. Thus, the effective conduction of Li-ion through the solid electrolyte domain is insufficient for electrodes containing highly active materials. Consequently, electrical conduction from the carbon additive is not the principal mechanism for improving the electrochemical performance of highly active material-containing electrodes. Whereas electron conduction within the electrode with a highly active material is feasible through interfaces such as active material-active material and carbon additive-active material, ionic conduction is hindered by the high volumetric occupation of the carbon additive in the solid electrolyte domain. Thus, the optimization of the carbon additive in a highly active material-containing ASSB electrode is crucial for achieving a high areal capacity design.

Spherical carbon additive (SC) content-dependent electrochemical characterization was performed and demonstrated in Figure 2. Voltage profiles at 0.05 C-rate applied show a decrease in polarization owing to the incorporation of carbon additives, indicative of enhanced electrical conductivity (Figure 2a). Conversely, increasing the carbon additive content to 3 wt% shows polarization growth, implying that the underlying failure mechanism at electrodes with high carbon additive-content. Figure 2b demonstrates the irreversible capacity developed during the initial formation cycle. A gradual increase in the irreversible capacity was observed according to the carbon additive composition. Whereas the electrode with 0 wt% exhibits an irreversible capacity of 26.3 mA h g⁻¹, the electrode containing 3 wt% SC dissipates 42.9 mA h g⁻¹, highlighting a higher occurrence of electrochemical side reactions at 3 wt% electrode. The rate capability test indicated an atypical behavior with the introduction of a carbon additive. Typically, a high degree of carbon additive incorporation is presumed to enhance rate capability. However, the rate performance test at the ASSB shows reverse conduct (Figure 2c). A comparison with the 0 wt% SC electrode demonstrates improved rate capability only with 1 wt% of SC; whereas cells containing 2, 3 wt% SC exhibits significant capacity degradation at higher C-rates. The corresponding voltage profiles show polarization growth at a high C-rate for cells with various SC-contented contents. (Figure S2, Supporting Information) Furthermore,

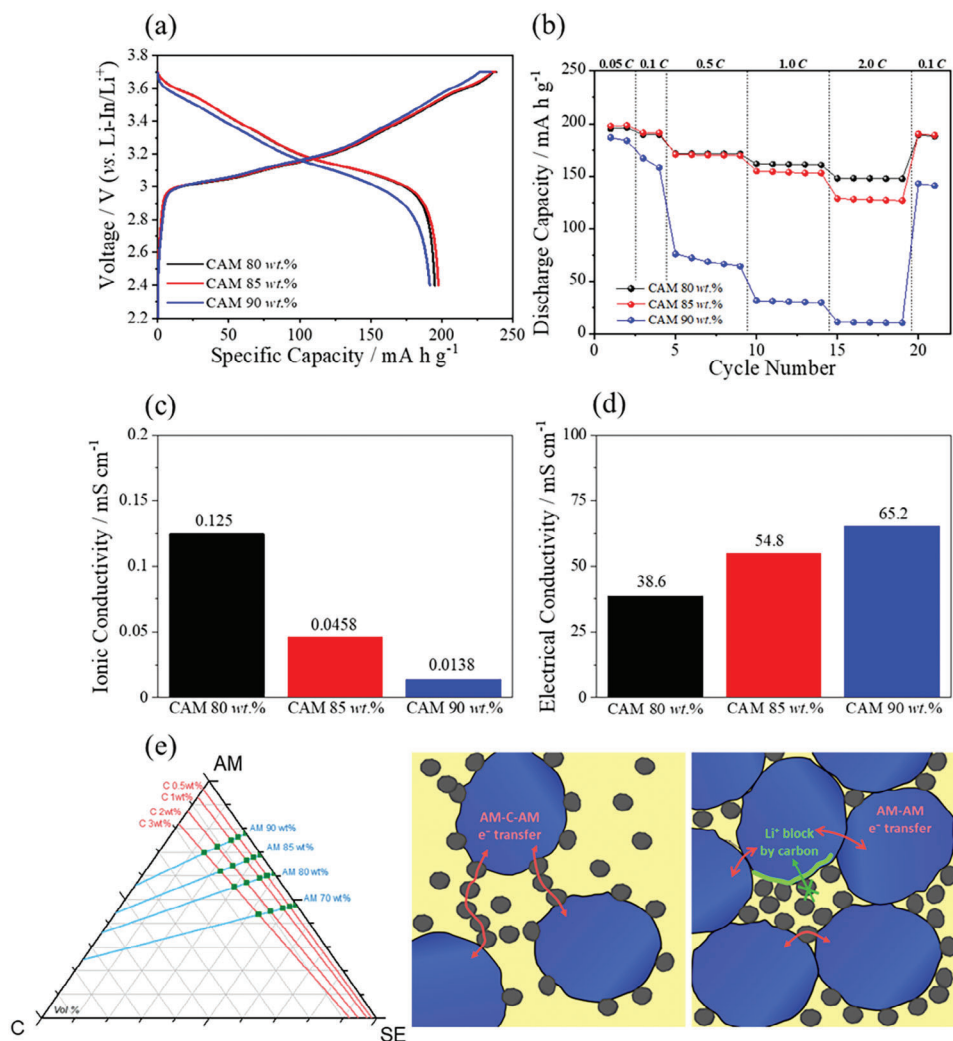


Figure 1. Positive active material portion-dependent cell performances at 3 wt% of carbon additive: a) formation voltage profiles at 0.05 C, b) rate performances, c) ionic, and d) electrical conductivity of electrode pellets, and e) volumetric occupation diagram and scheme illustrating the effect of carbon additive on three-compositional elements.

cycleability evaluation indicated substantial capacity deterioration with higher SC-contents, strongly correlated with the initial irreversible capacity (Figure 2d). At 0.5 C-rate cycle, stable cycle performance is observed with SC-free electrodes, while capacity degradation is crucial with SC exceeding 2 wt%. Furthermore, a high initial capacity degradation was observed with SC 3 wt% electrode.

Because the degradation of the electrochemical performance of ASSB is highly dependent on the initial irreversible capacity, the initial polarization development during the formation period was traced by applying a CC pulse at the corresponding voltage. Prior to pulse application, a 0.05 C charging was applied, followed by a 1.0 min of 1.0 C CC pulse and 10 min rest periods. The voltage versus polarization curves were individually characterized by solid electrolyte decomposition on the carbon additive and the NCM charge-transfer-incorporated range (Figure 2e). The previous study reports that the oxidation of sulfide-based solid electrolyte is occurred below the 3.2 V (vs Li-In/Li⁺),^[1h,8b,e] and thus the comparison of polarization was performed below 3.2 V and

after 3.2 V, respectively. The observed polarization in the ASSB demonstrates high resistance to solid electrolyte decomposition on the carbon additive step, implying that the decomposition of the solid electrolyte on the carbon additive induces the formation of a resistive layer upon the introduction of a high carbon additive. Furthermore, the resulting polarization growth was observed at the NCM charge transfer in the voltage region with SC 2 and 3 wt% electrodes at 3.4 to 3.7 V (vs Li-In/Li⁺) region. Thus, the oxidative decomposition of the solid electrolyte influences the charge transfer of the NCM electrode, which significantly deteriorates the power and cycle performance of ASSB electrodes. The *ex-situ* O 1s XPS spectra showed that the NCM active material (M–O, lattice oxygen^[3d,e,6d,e,10]) was shrouded by anodic decomposition products (sulfate,^[5b,c] phosphate,^[1e,5c,d,6a,11] and P–O–P^[8d]) from the solid electrolyte (Figure 2f). Although an identical voltage cut-off was applied to SC with 1 and 3 wt% electrodes, the decomposition of solid electrolytes varied significantly. Consequently, the interaction between the carbon-solid electrolyte and NCM surface is expected to result in significant polarization

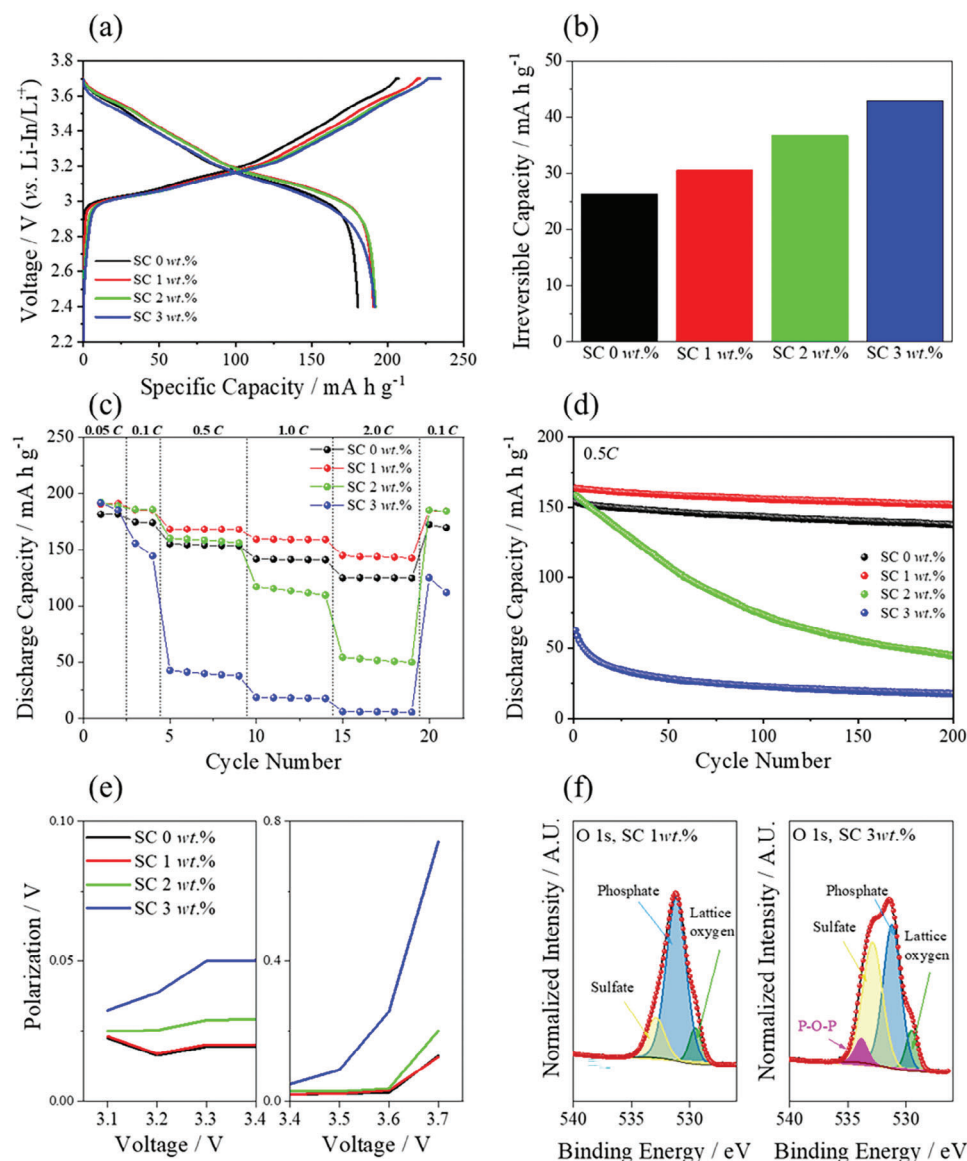


Figure 2. Carbon additive composition-dependent cell performances at 90 wt% of positive active materials: a) formation voltage profile 0.05 C, b) irreversible capacity at formation process c) rate performances, d) cycleability of electrode pellets, e) polarization growth during initial de-lithiation of NCM pellets with various carbon additive contents, and f) *post-mortem* O 1s XPS spectra after formation with 1 and 3 wt% of carbon additive.

growth with surplus SC incorporation. Additional P-O-P-based species were observed in the 3 wt% electrode, indicating severe solid electrolyte oxidation in cells with high carbon additive content. These species can be further oxidized as the phosphate compounds. It is noteworthy that the measured ionic conductivity of the pellet electrode was similar to that of the SC 1 to SC 3 wt%, while the electric conductivity is significantly increased with SC introduction. (Figure S3, Supporting Information) Hence it is expected that the carbon additive induces crucial degradation of the solid electrolyte due to the extremely high electrical conductivity of the pellet electrode.

Morphological characterization of the fabricated-electrode using focused-ion beam (FIB) cross-sectioned high-resolution transmission electron microscopy (HR-TEM) (Figure 3a) shows

the crucial occupation of the carbon additive within the solid electrolyte domain at SC 3 wt% electrode, while a solid electrolyte-contacted NCM surface is observed with SC 1 wt%. The line EDS profile shows that the NCM-solid electrolyte-carbon additive interfaces are evident at SC 3 wt%, comprising carbon from conductive additive, sulfur from solid electrolyte, and nickel signal from the NCM (Figure 3b). This three-phase contact interface catalyzes the anodic decomposition of solid electrolytes, initiating from the carbon surface and subsequently oxidizing on the NCM surface, forming, for instance, P-O-P species. Consequently, the significant polarization growth is due to the high carbon content in the pellet electrode. Figure 3c illustrates the failure scheme induced by the introduction of a high-carbon additive. At low carbon content, the Li-ion pathway is well preserved due to the

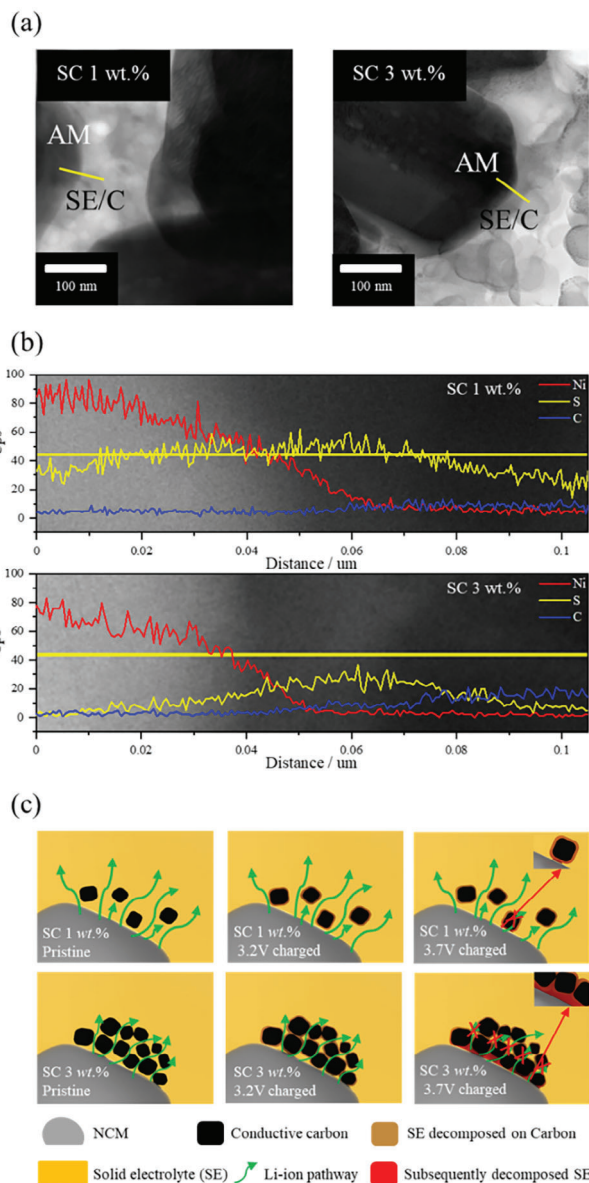


Figure 3. a) HR-TEM images of the FIB-processed 90 wt.% NCM incorporated pellet electrodes and b) line EDS profile of the active material and carbon-solid electrolyte domain interfaces with SC 1 and SC 3 wt% electrodes, c) scheme illustrating the effect of carbon additive on the decomposition of solid electrolyte.

increased volumetric fraction of the solid electrolyte, whereas the high-carbon-content electrode hinders Li-ion transport by carbon occupation in the solid electrolyte domain in the pristine state. Upon reaching 3.2 V (vs Li-In/Li⁺), oxidative decomposition on the carbon surface occurred and subsequent blocking of the Li-ion pathway was observed at the high-carbon-content electrode. Furthermore, the oxidized solid electrolyte on the carbon surface, observed at 3.7 V (vs Li-In/Li⁺), significantly degraded the interface of the NCM and the solid electrolyte. Consequently, it is essential to decrease the solid electrolyte-carbon contact volume in high-active-material-composition electrodes, implying the

critical role of morphological changes in the carbon additive for modulating high-areal-capacity electrodes.

To mitigate the volumetric occupation of the carbon additives in the solid electrolyte domain and the subsequent formation of the NCM-solid electrolyte-carbon interface, a carbon fiber (CF)-based conductive additive was introduced (Figure 4). Figure 4a depicts the morphological changes induced by the carbon additive on the electrode structure. SC additives tend to disperse widely throughout the electrode structure, particularly within the solid electrolyte domain, leading to electrochemical side reactions and suppressing ionic conduction. In contrast, the CF-containing electrode exhibits inter-particle connections due to its linear structure, thereby minimizing contact between the solid electrolyte and carbon additives. SEM images of SC and CF are illustrated in Figure S4 (Supporting Information). Thus, electrochemical side reactions can be effectively suppressed and the electrical conductivity of the dry electrode can be improved. Figure 4b illustrates the occupation of the SC and CF in the solid electrolyte domain with the carbon additive concentration set as 1 wt%. In the SC electrode, the carbon signal was widely dismantled in the solid electrolyte domain, hindering Li-ion transfer and facilitating the oxidative decomposition of the solid electrolyte. In contrast, the CF maintains interparticle connection within NCM owing to its intrinsic linear structure, resulting in minimized contact between the CF and the solid electrolyte (Figure 4b). Thus, the substitution of SC with CF is expected to improve electrochemical performance by suppressing side reactions while preserving electrical conductivity. Figure 4c shows the measured ionic and electrical conductivities of the dry electrodes with SC and CF additives, respectively. Enhanced ionic conductivity was observed due to the less-occupied carbon additive in the solid electrolyte domain. 22% of ionic conductivity was improved by substituting SC with CF. Furthermore, electrical conductivity remains consistent with the introduction of CF, attributed to well-preserved inter-particle connection within the dry electrode, as evidenced by the similar electrical conductivity.

A comparative analysis of the electrochemical side reactions of SC and CF was conducted at the dry electrode, followed by a *post-mortem* XPS analysis (Figure 5). The cyclic voltammetry with identical mass-comprising SC and CF indicated suppressed oxidation of the solid electrolyte on the carbon surface. The maximum oxidative current from the SC was 0.088 mA, while that from the CF was 0.015 mA, which was a significantly decreased value. (Figure S5, Supporting Information) Thus a suppressed anodic side reaction is expected with CF at identical mass application. In contrast, the current density calculated from the Brunauer-Emmett-Teller (BET) surface area indicates the similar oxidative decomposition rate was demonstrated from SC and CF additives (Figure S6, Supporting Information), implying that the volumetric occupation of the carbon additive in the solid electrolyte domain is critical to improve the electrode performances. The state-of-charge-dependent, *ex situ* S 2p XPS spectra indicate significant oxidation of the solid electrolyte at the SC electrode, compared with that at the CF electrode (Figure 5a,b). The formation of SO_x bonds is observed in SC, which is due to the reaction of the NCM solid electrolyte.^[5c,d] Thus, the catalyzed oxidation of the solid electrolyte was also confirmed by the state-of-charge-dependent XPS spectra. Figure 5c shows the rate capabilities of the SC and CF electrodes. The rate performance of CF is

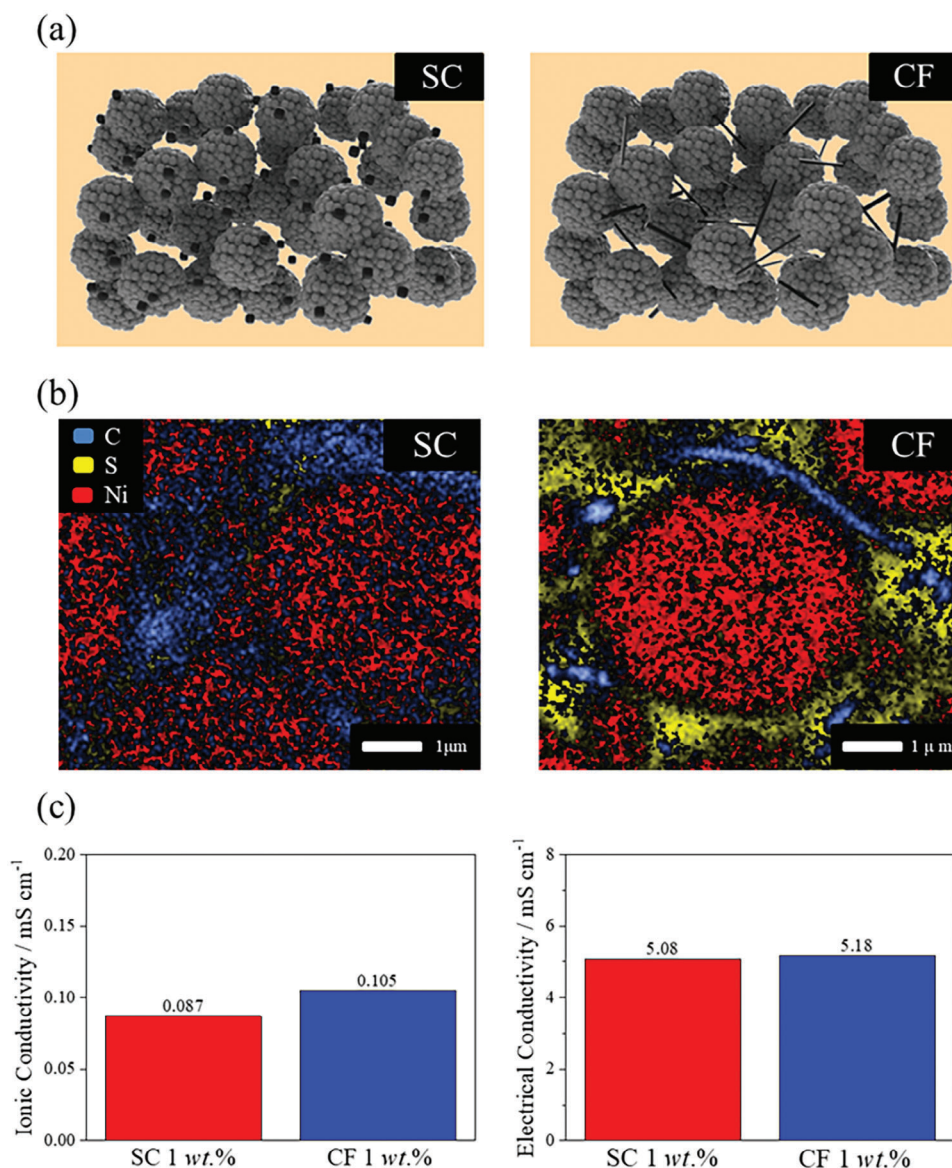


Figure 4. a) Schematic representation of the spherical carbon (SC) and carbon fiber (CF)-type additive comprised electrodes b) overlapped EDS map of fabricated dry electrode with C, S, and, Ni $K\alpha$ signal, c) measured ionic and electrical conductivity of SC and CF introduced dry electrodes.

highly improved by both the ionic and electrical conductivities, considering the electrode architecture, which is expected from the measured conductivity values (Figure 4c). The 0.2 C cycle performance test revealed that the suppressed side reaction from the decreased contact with the carbon-solid electrolyte improved the Coulombic efficiencies during cycling; hence, the capacity retention of the 6.0 mA h cm⁻² dry electrode was well retained after 150 cycles (Figure 5d). The cycle number-dependent voltage profiles are demonstrated at Figure S7 (Supporting Information). In SC-added cell, the gradual diffusion polarization growth with continued cycling was observed, implying that the interfacial deterioration of NCM electrode is significant with SC application. In contrast, the stable voltage profile was demonstrated with CF incorporation, which indicates the interface failure of NCM is mitigated with decreased electrolyte-carbon contact area.

Consequently, the utilization of properly morphologically designed carbon additives is crucial for realizing high-areal-capacity electrodes with high active material content. The demonstrated cycle performances with a high areal capacity electrode greatly surpass the recently reported results,^[12] and hence the importance of the carbon additive design is highly significant in modulating the electrochemical performance of high-energy ASSB electrodes.

3. Conclusion

This study unravels the interlinked oxidation phenomenon occurring in solid electrolytes, which triggers escalated oxidative degradation of the argyrodite solid electrolyte when in contact with the NCM surface. The oxidation of solid electrolytes on

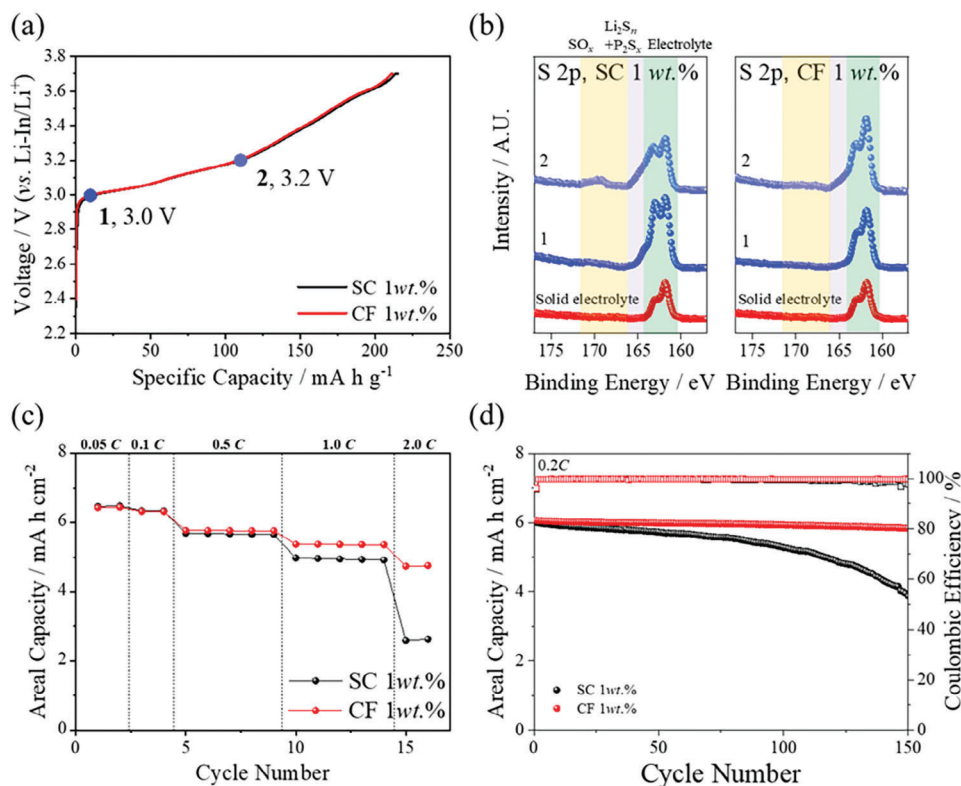


Figure 5. a) Initial voltage profiles for *ex-situ* analysis voltage points b) *post-mortem* S 2p XPS spectra dependent on state-of-charge at 3.0 and 3.2 V (vs Li-In/Li⁺), c) rate capability, and d) 60 °C cycle performance at 6.0 mA h cm⁻² areal capacity dry electrode with spherical carbon and carbon fiber additive.

conductive carbon substrates readily generates oxidative intermediates, thereby inducing immense oxidation on the NCM surface. The presence of solid electrolyte in the positive electrode and the retention of solid electrolyte post-NCM formation is reduced with the inclusion of high-weight-composition conductive carbon additives. Therefore, high-carbon-additive-content cells demonstrate a considerable decline in the cycle life and power capabilities of ASSBs. This fundamental failure mechanism caused by conductive carbon is primarily observed in cells with a high active material content, severely limiting the energy density of ASSBs. Consequently, this study offers critical insights into the design of high energy density ASSBs with practical electrodes composed of a high active material ratio and a Ni-rich material. Carbon fiber-type additives are employed to line-connect the active materials, mitigating ASSB failure caused by the high volumetric-occupied conductive carbon additive. Additionally, morphological modifications of the conductive carbon additives significantly enhance the electrochemical performance of ASSBs, suppressing electrolyte degradation and preserving electrode structure deterioration even after extended cycles.

Supporting Information

Supporting Information is available from the Wiley Online Library or from the author.

Acknowledgements

H.-S.K. and S.P. contributed equally to this work. This work was supported by the Ministry of Trade, Industry and the Energy/Korea Evaluation Institute of Industrial Technology (MOTIE/KEIT) (Nos. 20012330, 20026760).

Conflict of Interest

The authors declare no conflict of interest.

Data Availability Statement

The data that support the findings of this study are available from the corresponding author upon reasonable request.

Keywords

all-solid-state batteries, areal capacity, carbon additives, electrode design, sulfide electrolytes

Received: May 30, 2024
Revised: June 23, 2024
Published online: July 3, 2024

[1] a) Y. C. Jung, C. Hwang, M. J. Kwak, S. J. Jeon, Y. J. Lee, W. J. Kwak, H. S. Kim, K. Kim, W. S. Cho, J. S. Yu, *J. Mater. Chem. A* **2023**, *11*, 25275;

- b) J. Y. Jung, S. A. Han, H.-s. Kim, J. H. Suh, J.-S. Yu, W. Cho, M.-S. Park, J. H. Kim, *ACS Nano* **2023**, *17*, 15931; c) B. K. Park, H. Kim, K. S. Kim, H.-S. Kim, S. H. Han, J.-S. Yu, H. J. Hah, J. Moon, W. Cho, K. J. Kim, *Adv. Energy Mater.* **2022**, *12*, 2201208; d) H.-s. Kim, J. Y. Jung, K. Kim, C. Hwang, J. Yu, M.-S. Park, W. Cho, *Adv. Energy Mater.* **2024**, *14*, 2303965; e) S. Kang, H. S. Kim, J. Y. Jung, K. H. Park, K. Kim, J. H. Song, J. S. Yu, Y. J. Kim, W. Cho, *ACS Appl. Mater. Interfaces* **2023**, *15*, 10744; f) Y. Liang, H. Liu, G. Wang, C. Wang, Y. Ni, C.-W. Nan, L.-Z. Fan, *InfoMat* **2022**, *4*, e12292; g) Y. Pang, J. Pan, J. Yang, S. Zheng, C. Wang, *Electrochem. Energy Rev.* **2021**, *4*, 169; h) A. Banerjee, X. Wang, C. Fang, E. A. Wu, Y. S. Meng, *Chem. Rev.* **2020**, *120*, 6878; i) Y. Huang, B. Shao, F. Han, *Curr. Opin. Electrochem.* **2022**, *33*, 100933; j) F. Zheng, M. Kotobuki, S. Song, M. O. Lai, L. Lu, *J. Power Sources* **2018**, *389*, 198; k) H. Wan, J. Zhang, J. Xia, X. Ji, X. He, S. Liu, C. Wang, *Adv. Funct. Mater.* **2022**, *32*, 2110876.
- [2] a) X. Sun, Y. Yamada, S. Hori, Y. Li, K. Suzuki, M. Hirayama, R. Kanno, *J. Mater. Chem. A* **2021**, *9*, 17905; b) K. Kim, J. Park, G. Jeong, J.-S. Yu, Y.-C. Kim, M.-S. Park, W. Cho, R. Kanno, *ChemSusChem* **2019**, *12*, 2637; c) Y. Kato, S. Hori, T. Saito, K. Suzuki, M. Hirayama, A. Mitsui, M. Yonemura, H. Iba, R. Kanno, *Nat. Energy* **2016**, *1*, 16030; d) N. Kamaya, K. Homma, Y. Yamakawa, M. Hirayama, R. Kanno, M. Yonemura, T. Kamiyama, Y. Kato, S. Hama, K. Kawamoto, A. Mitsui, *Nat. Mater.* **2011**, *10*, 682; e) D. Y. Oh, K. T. Kim, S. H. Jung, D. H. Kim, S. Jun, S. Jeoung, H. R. Moon, Y. S. Jung, *Mater. Today* **2022**, *53*, 7; f) A. Sakuda, A. Hayashi, M. Tatsumisago, *Sci. Rep.* **2013**, *3*, 2261; g) J. Lau, R. H. DeBlock, D. M. Butts, D. S. Ashby, C. S. Choi, B. S. Dunn, *Adv. Energy Mater.* **2018**, *8*, 1800933; h) J. Y. Jung, K. Kim, J. H. Suh, H.-s. Kim, M. J. You, K.-H. Park, J. H. Song, J.-S. Yu, J.-W. Lee, W. Cho, M.-S. Park, *Chem. Eng. J.* **2023**, *470*, 144381; i) S. Dong, L. Sheng, L. Wang, J. Liang, H. Zhang, Z. Chen, H. Xu, X. He, *Adv. Funct. Mater.* **2023**, *33*, 2304371; j) S. Jing, H. Shen, Y. Huang, W. Kuang, Z. Zhang, S. Liu, S. Yin, Y. Lai, F. Liu, *Adv. Funct. Mater.* **2023**, *33*, 2214274.
- [3] a) H. s. Kim, T. H. Kim, W. Kim, S. S. Park, G. Jeong, *ACS Appl. Mater. Interfaces* **2023**, *15*, 9212; b) H.-s. Kim, T. H. Kim, S. S. Park, M. S. Kang, G. Jeong, *ACS Appl. Mater. Interfaces* **2021**, *13*, 44348; c) H.-s. Kim, J. Kim, S. T. Yoo, J. H. Ryu, S. M. Oh, *J. Electrochem. Soc.* **2021**, *168*, 040523; d) C. R. Lee, H. Y. Jang, H. J. Leem, M. A. Lee, W. Kim, J. Kim, J. H. Song, J. Yu, J. Mun, S. Back, H.-s. Kim, *Adv. Energy Mater.* **2024**, *14*, 2302906; e) M. A. Lee, H. J. Leem, J. B. Lee, C. Hwang, J. Yu, H.-s. Kim, *J. Mater. Chem. A* **2023**, *11*, 21244; f) T. H. Kim, S. H. Kim, S. S. Park, M. S. Kang, S. S. Kim, H.-s. Kim, G. Jeong, *J. Electrochem. Sci. Technol.* **2023**, *14*, 369; g) T. H. Kim, S. S. Park, M. S. Kang, Y. R. Kim, H. S. Park, H. S. Kim, G. Jeong, *J. Electrochem. Soc.* **2022**, *169*, 020562.
- [4] a) N. Lee, J. Lee, T. Lee, J. Oh, I. Hwang, G. Seo, H. Kim, J. W. Choi, *ACS Appl. Mater. Interfaces* **2023**, *15*, 34931; b) M. Metzger, C. Marino, J. Sicklinger, D. Haering, H. A. Gasteiger, *J. Electrochem. Soc.* **2015**, *162*, A1123; c) Y. Itou, N. Ogihara, S. Kawachi, *J. Phys. Chem. C* **2020**, *124*, 5559; d) M. E. Spahr, D. Goers, A. Leone, S. Stallone, E. Grivei, *J. Power Sources* **2011**, *196*, 3404.
- [5] a) H. Visbal, S. Fujiki, Y. Aihara, T. Watanabe, Y. Park, S. Doo, *J. Power Sources* **2014**, *269*, 396; b) K. Nie, Y. Hong, J. Qiu, Q. Li, X. Yu, H. Li, L. Chen, *Front. Chem.* **2018**, *6*, 616; c) J. Auvergnot, A. Cassel, J.-B. Ledeuil, V. Viallet, V. Seznec, R. Dedryvère, *Chem. Mater.* **2017**, *29*, 3883; d) R. Koerver, I. Ayygün, T. Leichtweiß, C. Dietrich, W. Zhang, J. O. Binder, P. Hartmann, W. G. Zeier, J. Janek, *Chem. Mater.* **2017**, *29*, 5574; e) F. Walther, R. Koerver, T. Fuchs, S. Ohno, J. Sann, M. Rohnke, W. G. Zeier, J. Janek, *Chem. Mater.* **2019**, *31*, 3745; f) C. Lin, Y. Liu, H. Su, Y. Zhong, X. Wang, C. Gu, J. Tu, *Adv. Funct. Mater.* **2024**, *34*, 2311564.
- [6] a) A. Sakuda, A. Hayashi, M. Tatsumisago, *Chem. Mater.* **2010**, *22*, 949; b) N. Ohta, K. Takada, I. Sakaguchi, L. Zhang, R. Ma, K. Fukuda, M. Osada, T. Sasaki, *Electrochem. Commun.* **2007**, *9*, 1486; c) F. Walther, F. Strauss, X. Wu, B. Mogwitz, J. Hertle, J. Sann, M. Rohnke, T. Brezesinski, J. Janek, *Chem. Mater.* **2021**, *33*, 2110; d) H. J. Leem, W. Kim, S. S. Park, J. Yu, Y. J. Kim, H. s. Kim, *Small* **2024**, *20*, 2304814; e) W. Kim, T. H. Kim, J. Yu, Y. J. Kim, K. J. Kim, H. s. Kim, *Adv. Funct. Mater.* **2023**, *33*, 2306068; f) H.-s. Kim, G. Jeong, H. J. Leem, M. A. Lee, J.-N. Lee, S.-G. Woo, J. Yu, *J. Mater. Chem. A* **2022**, *10*, 17659.
- [7] a) Y. B. Sim, H. Lee, J. Mun, K. J. Kim, *J. Energy Chem.* **2024**, *96*, 185; b) Z. Zhang, W. Jia, Y. Feng, R. Ai, J. Yu, X. Bie, X. Zhai, T. Jiang, S. Yao, F. Du, *Energy Environ. Sci.* **2023**, *16*, 4453; c) T.-T. Zuo, F. Walther, J. H. Teo, R. Rueß, Y. Wang, M. Rohnke, D. Schröder, L. F. Nazar, J. Janek, *Angew. Chem., Int. Ed.* **2023**, *62*, 202213228; d) K. Wang, Z. Liang, S. Weng, Y. Ding, Y. Su, Y. Wu, H. Zhong, A. Fu, Y. Sun, M. Luo, J. Yan, X. Wang, Y. Yang, *ACS Energy Lett.* **2023**, *8*, 3450.
- [8] a) K. Kim, T. Kim, G. Song, S. Lee, M. S. Jung, S. Ha, A. R. Ha, K. T. Lee, *Adv. Sci.* **2023**, *10*, 2303308; b) W. Zhang, T. Leichtweiß, S. P. Culver, R. Koerver, D. Das, D. A. Weber, W. G. Zeier, J. Janek, *ACS Appl. Mater. Interfaces* **2017**, *9*, 35888; c) S. Randau, F. Walther, A. Neumann, Y. Schneider, R. S. Negi, B. Mogwitz, J. Sann, K. Becker-Steinberger, T. Danner, S. Hein, A. Latz, F. H. Richter, J. Janek, *Chem. Mater.* **2021**, *33*, 1380; d) R. Zhao, G. Hu, S. Kmiec, R. Gebhardt, A. Whale, J. Wheaton, S. W. Martin, *ACS Appl. Mater. Interfaces* **2021**, *13*, 26841; e) F. Walther, S. Randau, Y. Schneider, J. Sann, M. Rohnke, F. H. Richter, W. G. Zeier, J. Janek, *Chem. Mater.* **2020**, *32*, 6123; f) G. Oh, M. Hirayama, O. Kwon, K. Suzuki, R. Kanno, *Chem. Mater.* **2016**, *28*, 2634.
- [9] a) F. Zhang, Y. Guo, L. Zhang, P. Jia, X. Liu, P. Qiu, H. Zhang, J. Huang, *eTransportation* **2023**, *15*, 100220; b) Y. Sakka, H. Yamashige, A. Watanabe, A. Takeuchi, M. Uesugi, K. Uesugi, Y. Orikasa, *J. Mater. Chem. A* **2022**, *10*, 16602; c) F. Zhang, Q.-A. Huang, Z. Tang, A. Li, Q. Shao, L. Zhang, X. Li, J. Zhang, *Nano Energy* **2020**, *70*, 104545; d) S. Yanev, H. Auer, R. Pertsch, C. Heubner, K. Nikolowski, M. Partsch, A. Michaelis, *J. Electrochem. Soc.* **2024**, *171*, 050530.
- [10] J. Byun, C. R. Lee, W. Kim, M. A. Lee, H. Y. Jang, C. Hwang, J. H. Song, J.-S. Yu, S. Back, K. J. Kim, H.-s. Kim, *Adv. Funct. Mater.* **2024**, *2401620*.
- [11] a) J. Lim, Y. Zhou, R. H. Powell, T. Ates, S. Passerini, L. J. Hardwick, *Chem. Commun.* **2023**, *59*, 7982; b) J. Zhang, C. Zheng, L. Li, Y. Xia, H. Huang, Y. Gan, C. Liang, X. He, X. Tao, W. Zhang, *Adv. Energy Mater.* **2020**, *10*, 1903311.
- [12] a) W. Jiang, X. Fan, X. Zhu, Z. Wu, Z. Li, R. Huang, S. Zhao, X. Zeng, G. Hu, B. Zhang, S. Zhang, L. Zhu, L. Yan, M. Ling, L. Wang, C. Liang, *J. Power Sources* **2021**, *508*, 230335; b) F. Zhao, J. Liang, C. Yu, Q. Sun, X. Li, K. Adair, C. Wang, Y. Zhao, S. Zhang, W. Li, S. Deng, R. Li, Y. Huang, H. Huang, L. Zhang, S. Zhao, S. Lu, X. Sun, *Adv. Energy Mater.* **2020**, *10*, 1903422; c) Z. Zhang, S. Chen, X. Yao, P. Cui, J. Duan, W. Luo, Y. Huang, X. Xu, *Energy Storage Mater.* **2020**, *24*, 714; d) X. Yang, Q. Sun, C. Zhao, X. Gao, K. R. Adair, Y. Liu, J. Luo, X. Lin, J. Liang, H. Huang, L. Zhang, R. Yang, S. Lu, R. Li, X. Sun, *Nano Energy* **2019**, *61*, 567.